Dual-band shared-aperture variable inclination continuous transverse stub antenna

Lu, Yunlong; You, Yang; You, Qingchun; Wang, Yi; Huang, Jifu

Link to publication on Research at Birmingham portal

Dual-Band Shared-Aperture Variable Inclination Continuous Transverse Stub Antenna

Yunlong Lu, *Member, IEEE*, Yang You, Qingchun You, Yi Wang, *Senior Member, IEEE*, and Jifu Huang

Abstract—This paper presents a dual-band shared-aperture variable inclination continuous transverse stub (VICTS) antenna with large beam coverage for both frequency bands. A novel hybrid radiating structure is introduced to enable approximately consistent initial beam direction at the boresight for both bands and therefore large beam coverage, by exciting different sets of the radiation elements at each of the two bands. The hybrid structure is formed of interlaced conventional CTS elements and those backed by double-ridge waveguide-slots. The latter suppresses the lower band while allowing the high band to radiate. This configuration allows maximum aperture reuse. A parallel-plate waveguide (PPW) diplexer combines the generated plane waves from the two bands to enable one-side excitation. Combined with the non-uniform slow-wave structure (SWS), optimized amplitude distribution is achieved across the two frequency bands, thereby improving the antenna efficiency. A prototype is designed, fabricated and measured for 12.25-12.75 GHz (Ku-band) and 19.6-21.2 GHz (K-band). The measured reflection coefficients are kept less than -11.5 dB during the beam steering. At the center frequencies of 12.5 and 20.4 GHz, the measured beam coverage of over ±49° and ±59° in elevation plane is demonstrated from a relative rotation angle of 40°. During the beam steering, the measured peak gain varies in the range of 26.1-21.1 dBi / 30.4-25.2 dBi at these two frequencies.

Keywords—Variable inclination continuous transverse stub (VICTS) antenna, dual-band shared-aperture, beam steering, large beam coverage.

I. INTRODUCTION

Beam steering antennas are widely used in satellite-on-the-move (SOTM) applications, and data transmission between base stations and cars or unmanned aerial vehicles [1]-[5]. With the explosive increase in the volume of transmitted data, higher frequency spectrum resources are introduced into the wireless systems [6]. Multi-band operation has become a trend. For example, multiple frequency bands (S-, C-, Ku-, K- and Ka-bands) have been allocated to satellite communications (SATCOM) [7]-[12]. Conventionally, separate antennas are used for different bands. This configuration occupies large total aperture size and significantly increases the cost and system complexity. Therefore, integrating multiple beam steering antennas into the same aperture is highly desirable in reducing the component count and enhancing aperture reuse efficiency [13]-[19]. To ensure long-distance and stable communication link between the satellite/base stations and the mobile objects, high antenna gain is also essential [20]-[23].

Hollow-waveguide (HW) based continuous transverse stub (CTS) antennas, because of their high gain and wideband characteristics, have emerged as a competitive high-performance antenna technology [24]-[28]. According to the feeding structure, CTS antennas can be categorized into series feed and corporate feed. For beam steering, the series-fed CTS antenna is preferred. CTS-based leaky wave antennas can achieve beam steering by varying the operating frequency [29]-[32]. However, it is mostly restricted to 1-D scanning and also requires demanding hardware support due to the wide occupied bandwidth [33].

Variable inclination CTS (VICTS) antenna can provide 2-D beam steering at a fixed frequency [34]-[37]. The beam can be steered by relative rotation between the radiating part and the feeding part in the horizontal plane. A V-band VICTS antenna was reported [35] with a beam coverage of 0°-60°. In [36], two sets of radiation stubs were added to improve the sidelobe levels (SLLs) during beam steering. For dual-band operation, a VICTS antenna was excited by two independent feed networks in [37], with a flexible frequency ratio (FR). However, restricted by the same period of the radiation slots for the two bands, the beam coverage of the two bands was not identical, with the high band over 60° (from 8° to 68°) and the low band only over 38° (-35° to -73°). In [38], the authors reported a Tx/Rx dual-band VICTS antenna with consistent beam direction. However, the apertures of the two bands are independent and combined so the aperture area is not reused.

This paper proposes a dual-band shared-aperture beam steering antenna with maximum aperture reuse. It is a HW based VICTS antenna. Its main features include: (i) A new hybrid radiating structure overcomes the disadvantage of previous dual-band shared-aperture VICTS antenna [37] with equal radiation element periods at the two bands. This work achieves the dual-band shared-aperture operation with a large beam coverage of over 49° for both bands. (ii) Parallel-plate
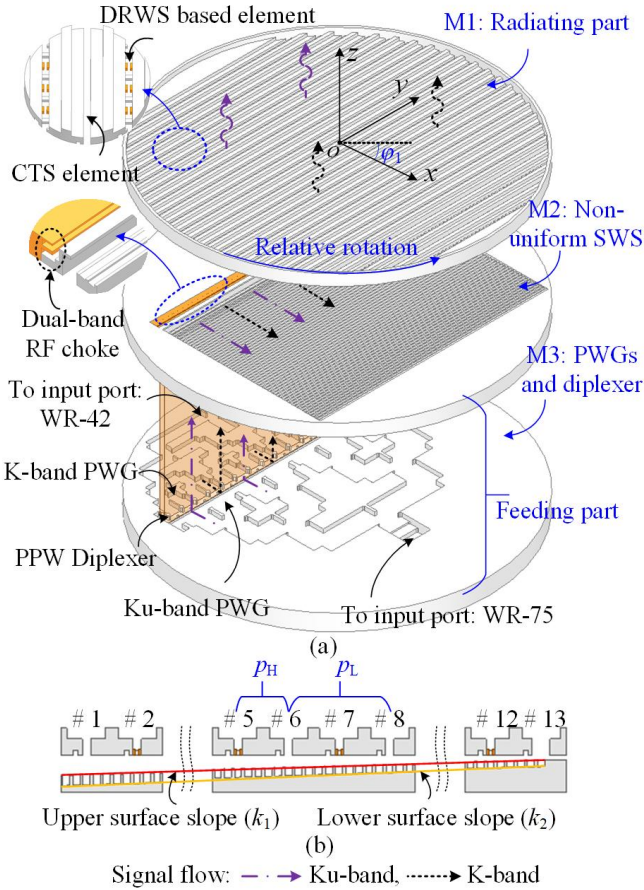
Fig. 1. Antenna configuration. (a) 3-D view; (b) side view of radiation elements within the region backed by SWS.
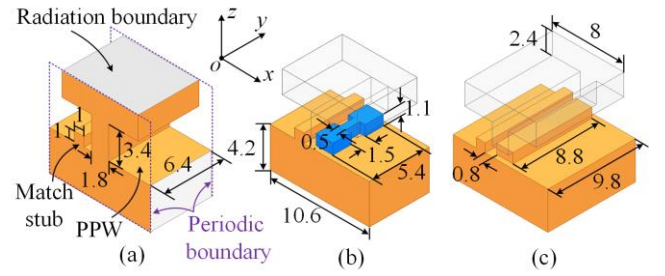

Fig. 2. Air model of the radiation unit. (a) Conventional CTS element unit; (b) DRWS unit; (c) rectangular waveguide-slot unit. For clarity, the DRWS section in (b) is highlighted in blue. All dimensions are given in millimeters.

non-uniform SWS to control the amplitude and phase distribution across the long radiation slots at both bands, two plane wave generators (PWGs) and a PPW diplexer (with a dual-band RF choke). The diplexer combines the quasi-TEM waves from the two PWGs to excite the radiation elements in series from one side. This helps to trade off the amplitude distributions of the excitation signal among the radiation elements in different frequency bands. The signal flows for the two bands are illustrated in Fig. 1. Two standard input waveguide ports (WR-42 for K-band and WR-75 for Ku-band) are located at the back side of the antenna. All the simulation results are performed by using Ansys HFSS. The design of the individual parts will be discussed next.

III. DESIGN AND ANALYSIS

A. Dual-band Radiation Slots

The key innovation in this design is the new topology of radiating slots that support the dual band in a shared aperture and with consistent initial beam direction between the two bands. A total of 13 long radiation slots are used (backed by the SWS). As shown in Fig. 1(b), there are two interlaced sets. The odd-number elements #1, #3, … are the conventional long CTS slots whereas the even-number elements #2, #4, … are those backed by the DRWSs. These even-number elements are used to suppress the low band as they are designed to have a cut-off frequency between the low and high band. When the operating frequency is at Ku-band (below the cut-off frequency), only the odd-number CTS elements radiate. When the operating frequency is at K-band (above the cut-off frequency), all the radiation elements radiate. In this way, the effective period (p_L) of the radiation elements in Ku-band is twice the effective period (p_H) in K-band, as illustrated in Fig. 1(b). p_L and p_H are chosen to avoid grating lobes. In this design, p_H is 0.75λ_H (10.6 mm) where λ_H is the free-space wavelength at the highest operating frequency in K-band. p_L is 21.2 mm (0.9λ_L where λ_L is the free-space wavelength at the highest operating frequency in Ku-band). The different effective periods for the two bands allow the initial beam directions to be set at around θ=0° (z-direction) for both bands (seen Section III-B). This in turn enables a large beam steering range for both bands.

The basic units of the conventional CTS element and the DRWS configuration are shown in Fig. 2(a) and (b). The CTS unit is a stepped flared continuous-slot structure, with a matching stub to reduce the reflection. The DRWS unit is similar to the CTS unit, except for a double-ridge waveguide

II. ANTENNA CONFIGURATION

The two concerned frequency bands in this work are 12.25 - 12.75 GHz (Ku-band) and 19.6 - 21.2 GHz (K-band). The whole antenna structure is shown in Fig. 1. It consists of the radiating part in layer M1 and the feeding part in layers M2 and M3. The radiating part is a hybrid structure with interlaced conventional CTS elements and those backed by the so-called 'double-ridge waveguide-slots (DRWSs)' (to be discussed in detail). When the relative rotation angle (φ_1) increases, the beam can be steered in the upper half space. It is worth mentioning that the beam directions of the VICTS antenna change in both elevation and azimuth planes during the beam steering [35], [37], [38]. The feeding part composes of a

waveguide (PPW) diplexer is designed to combine the plane waves at the two bands to excite the radiation elements from one side. By combining with the non-uniform slow-wave structure (SWS) [31], [38], optimized amplitude distribution among the radiation elements is obtained. It ensures a high total efficiency of over 82.3% in both bands. Compared with work [38], apart from the more efficient reuse of the aperture, this design achieves wide beam coverage. The paper is organized as follows: Section II describes the antenna configuration and Section III presents the detailed analysis and design. Section IV gives the experimental validation, followed by a conclusion in Section V.
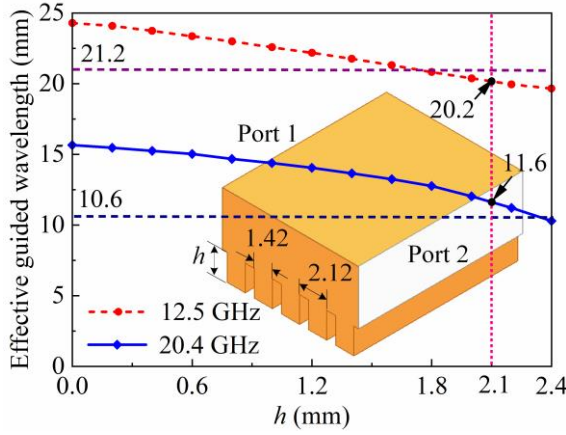
Fig. 3. Simulated effective guided wavelengths with different values of SWS depth (h) at the center frequencies of the two bands (12.5 and 20.4 GHz).
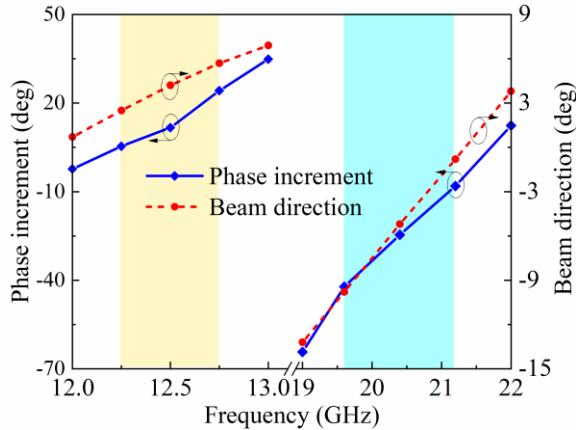

Fig. 4. Simulated phase increment between the adjacent radiation elements and beam directions of the initial beams (h=2.1 mm).

embedded between the flared slot structure and the PPW as shown in Fig. 2(b). The double-ridge waveguide is designed to have a cut-off frequency at 17 GHz in between the two bands so that it suppresses the Ku band. This can be achieved by adjusting its width. The optimized dimensions are given in Fig. 2.

A rectangular waveguide-slot could also generate the same cut-off characteristic. However, it would require a longer slot (8.8 mm) than that of the double-ridge one (5.4 mm), as shown in Fig. 2 (b) and (c) for comparison. This would have extended the spacing between adjacent waveguide slots, along the same row, to 9.8 mm (~ 0.67 λ_{HC}, λ_{HC} is the free-space wavelength at 20.4 GHz). Because of the 2-D beam-scanning characteristic of the VICTS antenna [38], this spacing would result in a large gain drop at large beam steering angles. It is also important to note that there is a mode conversion from quasi-TEM (PPW) to TE$_{10}$ (waveguide slot) and back to quasi-TEM (long radiation slot). The increased spacing would also decrease the conversion efficiency [31], thereby disrupting the amplitude distribution across the radiation elements (resulting in grating lobes). For these reasons, the DRWS is adopted here.

B. Slow-Wave Structure (SWS)

To obtain a wide beam steering range, the initial beam directions are optimized to be at the boresight around θ=0° (z-direction) for both bands. This is achieved by using a SWS.

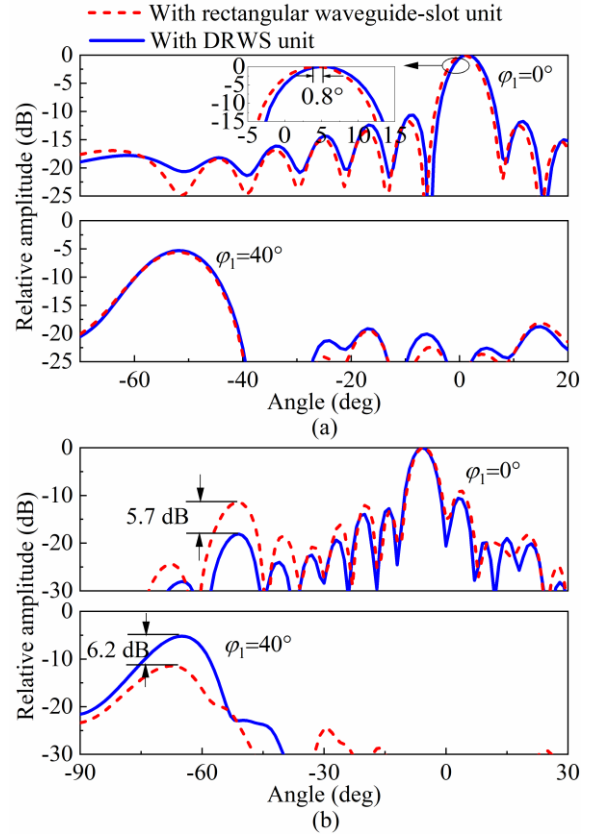Fig. 5. Normalized radiation performance in H-plane with φ_1=0° and φ_1=40° at (a) 12.5 GHz and (b) 20.4 GHz.

A uniform-SWS is shown in Fig. 3. By increasing the corrugation depth (h), the effective guided wavelength in the SWS-loaded PPW can be reduced [35]. The effective guided wavelengths corresponding to different SWS depths at the center frequencies of the two bands are also illustrated in Fig. 3. Perfect magnetic conductor (PMC) boundaries are used on the two sides of the SWS in simulation. For boresight radiation of the initial beam, the effective waveguide wavelengths at 12.5 and 20.4 GHz should be equal to the effective periods of the radiation slots (p_L of 21.2 mm and p_H of 10.6 mm, respectively). As can be seen from Fig. 3, this would require different SWS depths (approximately 1.7 mm and 2.35 mm, respectively). In this design, a compromised value of h=2.1 mm is chosen to balance the initial beam directions between the two bands. The corresponding effective guided wavelengths are 20.2 mm (12.5 GHz) and 11.6 mm (20.4 GHz), respectively, as marked in Fig. 3. Fig. 4 depicts the phase increment (without relative rotation, i.e., φ_1=0°) between the adjacent radiation elements with SWS loading and the initial beam directions. A phase increment of 11.7° at 12.5 GHz and -24.6° at 20.4 GHz is achieved, which in turn enables the initial beam directions at 4.2° and -5.2°. They are both slightly off the boresight because of the compromise made. Across the two bands, the variation of the initial beam direction with frequency is within 10°, ensuring a large steering range.

With the initial beam direction determined, the amplitude and phase distribution of the array elements will be considered next. The design drive here is a maximum antenna efficiency. It requires an amplitude distribution as uniform as possible across
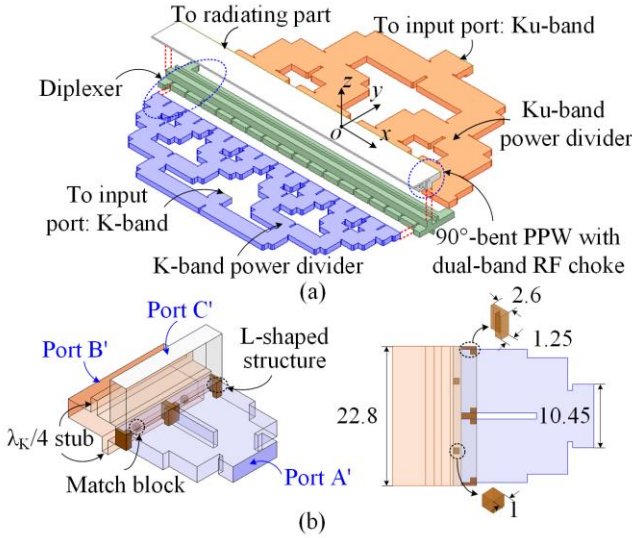
Fig. 6. Air model of the feed network. (a) Layout of the whole structure; (b) PPW diplexer unit. All dimensions are given in millimeters.
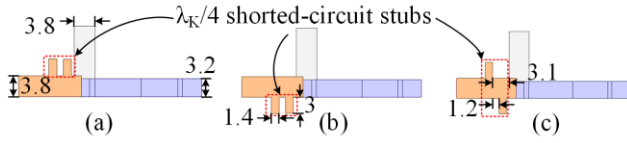

Fig. 7. Different configurations of the rejection shorting stubs. (a) Both on upper surface; (b) both on lower surface; (c) one per side. All dimensions are given in millimeters.

the array elements in both bands. This is realized by using a non-uniform SWS to control the power entering each radiating slot. As shown in Fig. 1(b), the slopes (k_1 and k_2) of the upper and lower surfaces of the SWS are adjusted [31]. Due to the different sets of radiation elements excited at Ku- and K-bands, two sets of slope values are ideally required. However, to balance the aperture efficiency in both bands, a compromise is made with one set of slope values. The influence of non-uniform SWS on phase distribution has also been considered. The optimized slope values are: k_1=0.0237 (1.36° tilt angle) and k_2=0.03 (1.72° tilt angle) in this design. This non-uniform SWS enables high aperture efficiencies in both bands, to be demonstrated in Section IV.

Fig. 5 shows the beam steering performance in H-plane with the relative rotation angle φ_1=0° and φ_1=40° at 12.5 and 20.4 GHz. The 3-dB beamwidth of the initial beam at 12.5 GHz is 8.5° and the sidelobe level (SLL) is -11.7 dB. At φ_1=40°, the beam points to -52° with a gain drop of 5.2 dB. The SLL is still below -12.6 dB. For the initial beam at 20.4 GHz, the 3-dB beamwidth is 5.2° and the SLL is less than -10. 5 dB. The beam is shifted to -67° with a gain drop of 5.3 dB at φ_1=40°. For comparison, the radiation performance based on the rectangular waveguide-slot unit is also plotted in Fig. 5(b). At 20.4 GHz, the grating lobe in the initial beam at -51° is raised by 5.7 dB, and the peak gain drop at φ_1=40° is increased by 6.2 dB. The deterioration in K-band radiation validates previous analysis against utilizing the rectangular waveguide-slots. The rectangular slots make little difference to the Ku-band, except that the initial beam is shifted by 0.8°, as shown in Fig. 5(a).
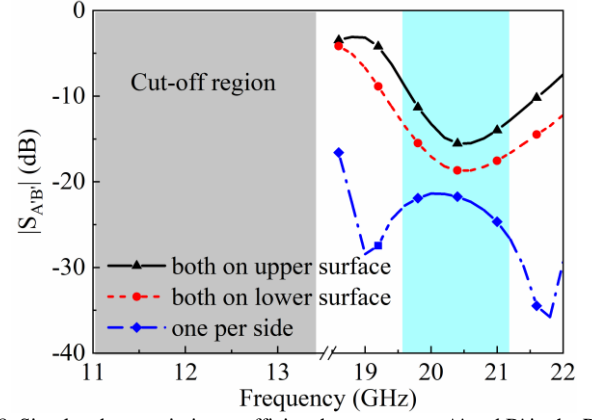
Fig. 8. Simulated transmission coefficient between ports A' and B' in the PPW diplexer unit in Fig. 6(b).
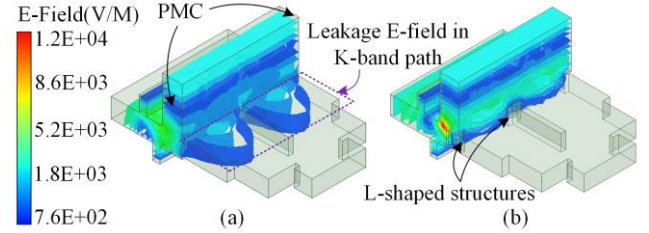
Fig. 9. E-field distribution in the diplexer unit at 12.5 GHz: (a) without L-shaped matching structure; (b) with L-shaped structure.
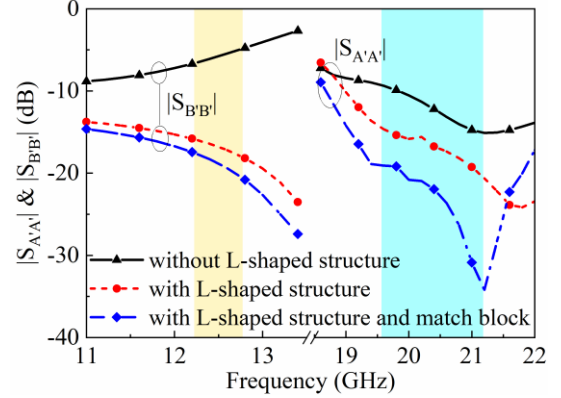
Fig. 10. Simulated reflection coefficients of the PPW diplexer unit.

C. PWGs and Diplexer in Layer M3

To achieve one-side excitation, the feed network employs a PPW diplexer to combine the plane waves separately generated in Ku- and K-bands. The layout of the feed network is shown in Fig. 6. For maximum antenna efficiency, the amplitude and phase of the plane waves generated should conform to a uniform and in-phase distribution. The Ku-band PWG is fed by a 1-to-8 H-plane, equal and in-phase power divider, whereas the K-band PWG is fed by a 1-to-16 divider. This type of PWG has compact size, wideband, and controllable amplitude distribution [32]. The design details of the H-plane T-junction dividers have been discussed in the previous work [37], and will not be repeated here.

The enlarged 3-D view of the PPW diplexer unit (one-eighth of the overall structure) is shown in Fig. 6(b). Port A' is for the K-band channel, Port B' is for the Ku-band. The two channels are combined to Port C'. The high-pass nature of the high band (K-band) provides the nature rejection to the low (Ku-) band.

Fig. 11. Partial structure of the 90°-bent PPW with RF chokes. (a) 3-D view; (b) side view. All dimensions are given in millimeters.

Fig. 12. Simulated blocked frequency response in K-band with different stub lengths shown in Fig. 11(b). (a) $|S_{AA}|$; (b) $|S_{CA}|$.

Fig. 13. Amplitude distributions of E-fields at (a) 12. 5 GHz and (b) 20.4 GHz.

Fig. 14. Transition waveguide bends structures and simulated results. All dimensions are given in millimeters.
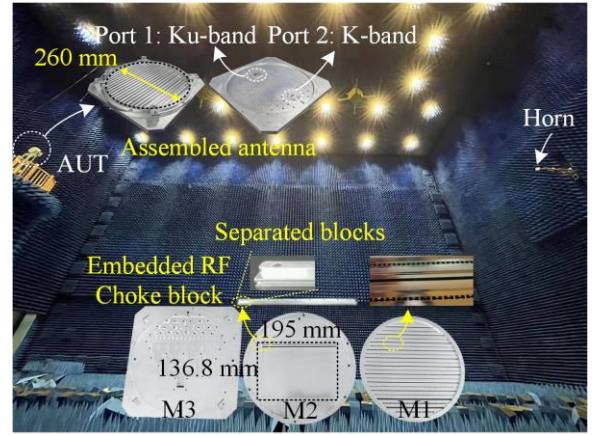
Fig. 15. Photographs of separated metal blocks, assembled antenna and test environment.

For the low band channel, however, two $\lambda_K/4$ (λ_K is the guided wavelength at the center of the K-band) stu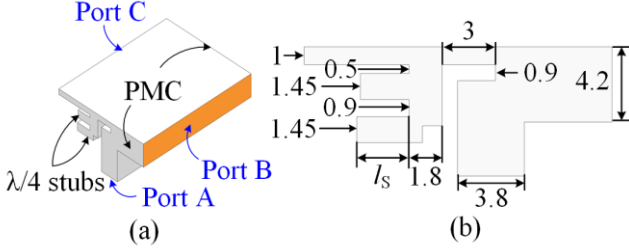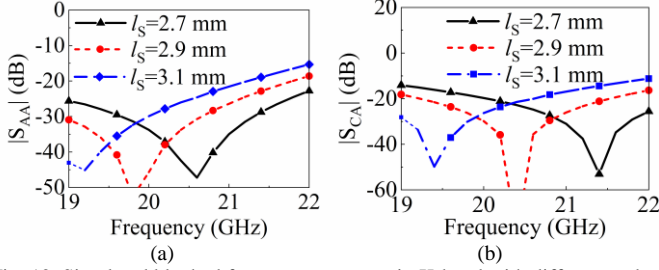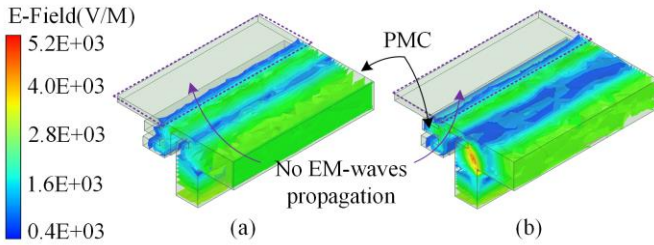bs are added to reject the high band and therefore ensure isolation. Among the three possibly different configurations of the two stubs, as shown in Fig. 7, we have found that loading the stubs from both side gives the highest isolation of over 21 dB as shown in Fig. 8. So this configuration has been used in the design.

However, in this configuration, at the low band frequency, the signal spills over to the K-band channel as shown by the field distribution in Fig. 9(a). This affects the impedance matching in both bands. To solve this, two L-shaped matching structures are added (see Fig. 6(b)). This further increases the K-band cut-off frequency (increasing the attenuation of the Ku-band). As evidenced by Fig. 9(b), the field spillage is reduced. The reflection coefficients with and without the L-shaped structures is compared in Fig. 10. The impedance matching in both Ku- and K-bands is improved. To further enhance the matching in K-band, a small block is added to the middle of the output port of the K-band power divider (Fig. 6(b)). The improvement is evident from Fig. 10.

The PPW at the output of the diplexer is bent by 90° in order to feed in series the radiating elements. A dual-band RF choke is used here to suppress any unwanted propagation in the opposite direction. The enlarged view of the RF choke and optimized dimensions, as well as the definition of the port

number, are shown in Fig. 11. The branch at port C represents the signal path caused by the spacing (about 1 mm air gap) left between the radiating layer and the SWS layer to allow free rotation. Signal leakage from this path should be suppressed to avoid unintended excitation of the radiation elements outside the region backed by the SWS. The choke is again realized by two $\lambda/4$ stubs, for Ku and K-band respectively. Take the K-band choke as an example. Fig. 12 shows that when l_S=2.9 mm, 20.4 GHz is blocked. In the frequency range of 19.6-20.4 GHz, $|S_{AA}|$ <-24 dB and $|S_{CA}|$<-23 dB. Fig. 13 shows the E-field distribution at 12.5 and 20.4 GHz, illustrating the choke effect.

A three-step waveguide bend is connected to the input port of both power dividers as a transition from the standard waveguide port to the H-plane waveguide. The structures with optimized dimensions, as well as the simulated S-parameters are plotted in Fig. 14.

IV. EXPERIMENTAL RESULTS

The prototype was milled from an aluminum-magnesium alloy (nominal conductivity of 3.8×10^7 S/m) with a manufacturing tolerance of 20 μm. It should be noted that the dual-band RF choke is separately fabricated and embedded in the layer M2. The metal blocks, assembled antenna and the test environment are shown in Fig. 15. The antenna is 260 mm in

Fig. 16. Simulated and measured S-parameters. (a) $|S_{11}|$ in Ku-band; (b) $|S_{22}|$ in K-band; (c) $|S_{21}|$.

diameter and 35 mm in height. The radiation performance is measured using a far-field test system in an anechoic chamber.

A. Reflection Coefficient

The simulated and measured reflection coefficients for the two bands at different relative rotation angles (φ_1) 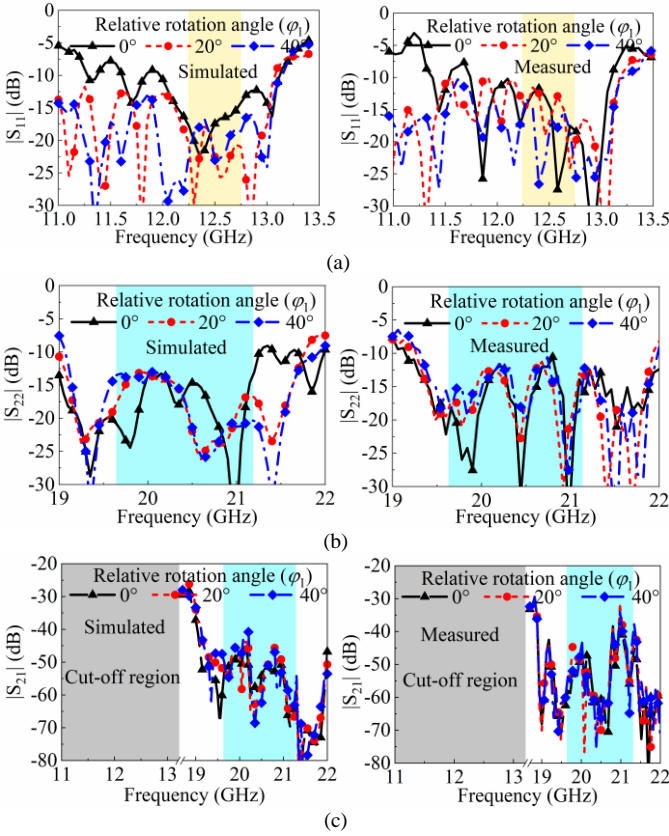are plotted in Fig. 16. The measurement was done using an Agilent E8361C network analyzer. The small difference between simulated and measured results is mainly due to manufacturing tolerances and assembly errors. When port 1 (Ku-band) is excited, the measured $|S_{11}|$ is less than -11.7 dB over 12.25-12.75 GHz for φ_1 from 0° to 40°. When port 2 (K-band) is excited, this is less than -11.5 dB over 19.6-21.2 GHz for the same rotation range. This demonstrates that the antenna exhibits wideband and stable impedance matching during beam steering. The simulated and measured isolations between the two ports are shown in Fig. 16(c). At different rotation angles, the measured $|S_{21}|$ is kept below -32 dB.

B. Radiation Performance

The simulated results of the main beam at different angles of φ_1 at 12.5 and 20.4 GHz are shown in Fig. 17. The beams at the two frequencies can both be steered in the upper half space (the so called 2-D steering). Note that the initial beams ($\varphi_1=0°$) deviate slightly from $\theta=0°$ (z-direction), as a result of the compromised SWS depth chosen as predicted from Fig. 4. For clarity, the beam scanning contours at the two frequencies are also plotted in Fig. 17. For a VICTS antenna with a relative rotation angle of φ_1, the beam direction (θ, φ) can be calculated
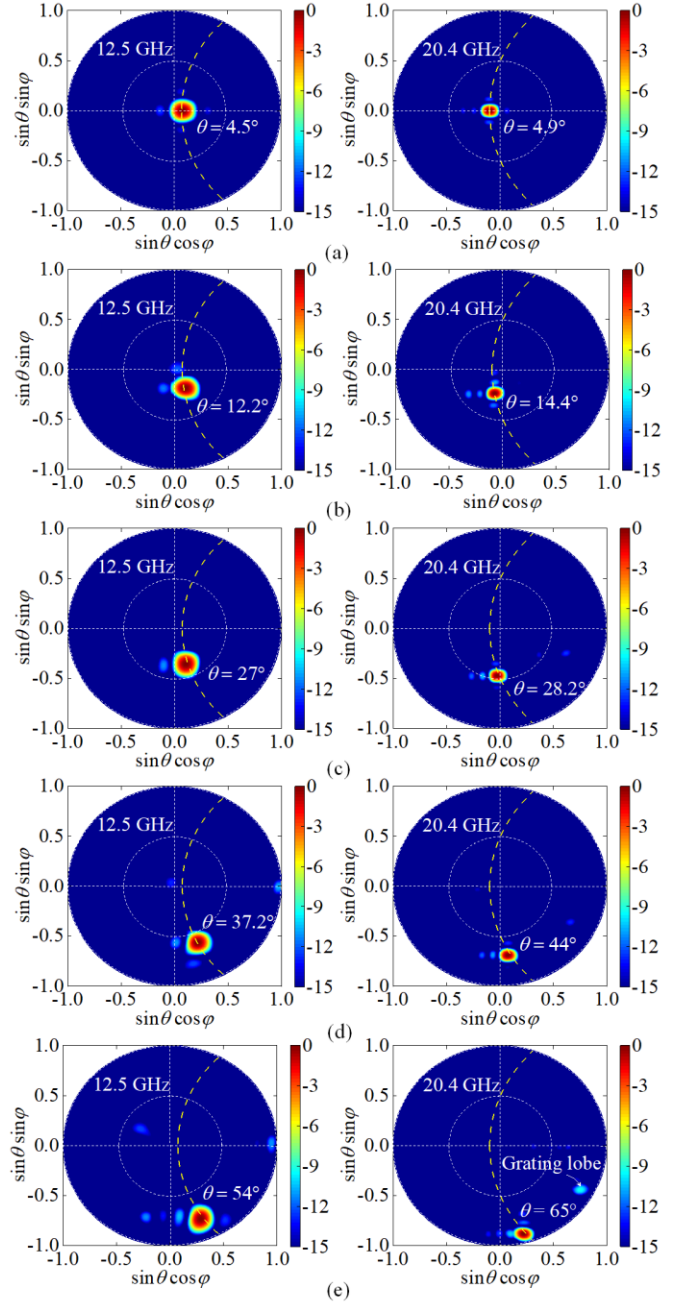
Fig. 17. Simulated 2-D plot of the radiation patterns with different values of φ_1 at 12.5 and 20.4 GHz. (a) $\varphi_1=0°$; (b) $\varphi_1=10°$, (c) $\varphi_1=20°$; (d) $\varphi_1=30°$, (e) $\varphi_1=40°$. Yellow dashed line is the beam scanning contour. The unit of the color bar is dB.

by using the following equations [35], [38]:

$$\left(\frac{\lambda_g}{\lambda_0}\right)^2 \sin^2(\theta) = \left[\cos(\varphi_1) - \frac{\lambda_g}{P}\right]^2 + \sin^2(\varphi_1) \qquad (1\text{-}1)$$

$$\tan(\varphi) = \frac{\sin(\varphi_1)}{\cos(\varphi_1) - \frac{\lambda_g}{P}} \qquad (1\text{-}2)$$

where λ_g and λ_0 are the effective guided wavelength and free-space wavelength, respectively, and P is the period of the radiation slots. The scanning contours can be obtained using the
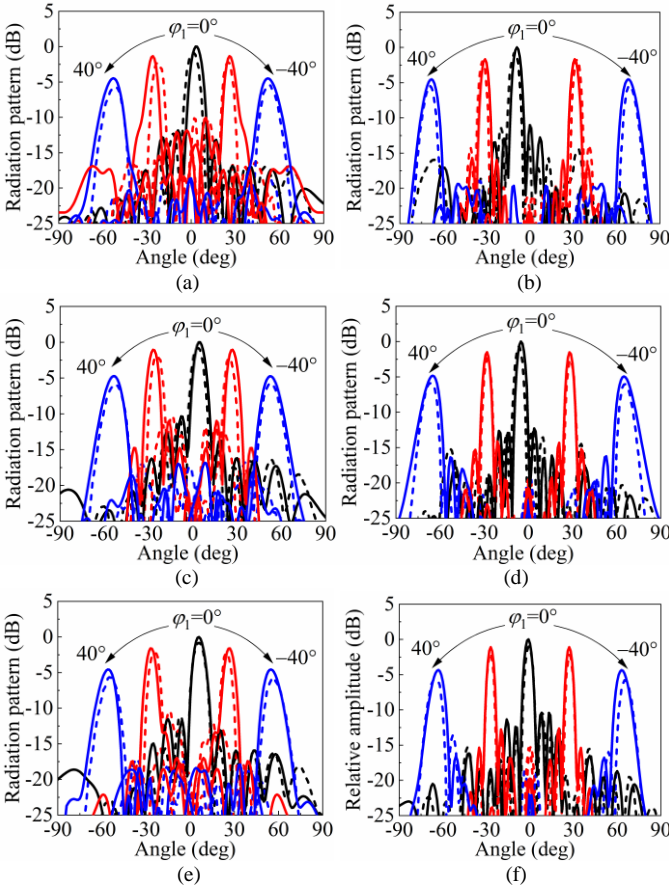
Fig. 18. Simulated and measured normalized radiation patterns in H-plane. (a) 12.25 GHz; (b) 19.6 GHz; (c) 12. 5 GHz; (d) 20.4 GHz; (e) 12.75 GHz; (f) 21.2 GHz. Dashed line: measurement; solid line: simulation.

Fig. 19. Simulated and measured peak gain with different φ_1.
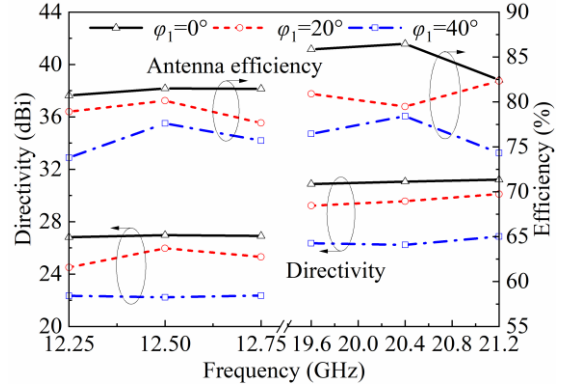
Fig. 20. Simulated directivity and antenna efficiency with different φ_1.

effective guided wavelengths and effective periods of radiation slots at 12.5 and 20.4 GHz, given in Section III.

From Fig. 17, it can be seen that the simulated main beam directions during beam steering closely match the respective scanning contours. The large coverage of 49.5°/60.1° can be achieved in elevation plane by changing the relative rotation angle from $\varphi_1=0°$ to $\varphi_1=40°$. A grating lobe appeared at 20.4 GHz with $\varphi_1=40°$, but is suppressed by about 10 dB. Due to the symmetrical structure, the opposite direction of beam steering can be obtained by changing the relative rotation direction. The simulated and measured normalized radiation patterns in H-plane at different relative rotation angles are shown in Fig. 18. A reasonably good agreement between simulation and measurement is achieved. For Ku-band, the measured/ simulated beam directions of the initial beam ($\varphi_1=0°$) at 12.25, 12.5 and 12.75 GHz point to 1°/3°, 4°/4.5°, and 6°/6°. At $\varphi_1=40°$ (-40°), the beam directions at these three frequencies are -52° (52°)/-53° (53°), -53° (53°)/-54° (53.6°), and -55° (56°)/-56° (54.4°), respectively. For K-band, the measured/ simulated initial beam directions at 19.6, 20.4 and 21.2 GHz are -10°/-9°, -6°/-4.9°, and -1/-1°, while these are -69° (68°)/-68° (67.8°), -66° (66°)/-65° (65.4°), and -65° (65°)/-63° (63.4°) at $\varphi_1=40°$ (-40°). The discrepancy between the simulations and measurements is within 2°. The maximum value appears at 12.75 and 21.2 GHz with $\varphi_1=40°$. This slight difference is mainly attributed to the simulation accuracy, manufacturing
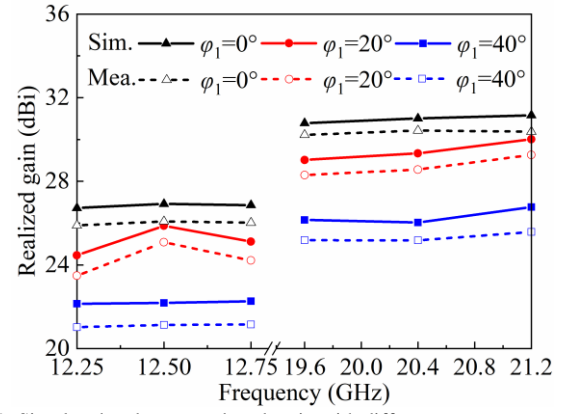
tolerances, assembly and measurement errors. The measured SLLs in Ku- and K-bands are both less than -10.5 dB during the beam steering.

Fig. 19 presents the simulated and measured peak gain at $\varphi_1=0°$, 20°, and 40°. The measured peak gain varies from 26.1 - 21.1 dBi and 30.4 - 25.2 dBi at 12.5 and 20.4 GHz, respectively, while the simulation values are in the range of 26.9-22.2 dBi and 31-26.1 dBi. The maximum difference between the simulated and measured peak gains for the initial beams is about 0.8 dB. This could be due to: (i) radiation pattern envelope and impedance matching variations, (ii) EM-field leakage between the metal layers, and (iii) measurement errors. During the beam steering, this gain difference raises to about 1.1 dB. This is attributed to the radiation pattern envelope deterioration and possibly increased EM-field leakage. The measured gain drops in Ku- and K-bands during the beam steering are within 5.2 dB and 5.3 dB. The simulated directivities at different relative rotation angles are shown in Fig. 20. The simulated directivity at 12.5 and 20.4 GHz varies in the range of 27-22.2 dBi and 31.1-26.2 dBi.

The antenna efficiency is calculated by using the measured peak gain and the simulated directivity, which is also shown in Fig. 20. It is higher than 73.8% and 74.3% in Ku- and K-bands during the beam steering. From the entire physical antenna aperture size, the simulated maximum aperture efficiency is 42.9% / 41.3% at 12.5 GHz / 20.4 GHz. This relatively small aperture efficiency is as result of the reduced effective radiation aperture. Commonly, the effective radiation aperture is the region supported by the excitation signal. That is the

TABLE I
PERFORMANCE COMPARISONS OF VICTS ANTENNAS

Ref.	Antenna structure	Center frequency (GHz)/ FBW (%)	Beam coverage	Aperture size (λ_0^2)[1]	Gain (dBi)	Isolation (dB)	Aperture efficiency (%)	Dual-band shared-aperture
[34]	HW-VICTS	12/16%	±56°	D=12	30.1	-	67.4	No
[35]	HW-VICTS	61.5/13%	±60°	D=11.6	29.3	-	77	No
[37]	HW-VICTS	19.8/3% 29.2/2.7%	±38° ±60°	L[2]:7.3×6.5 H: 10.8×9.7	24.3 28.5	>20	45.8 55	Yes
[38]	HW-VICTS	20/10% 30/6.7%	±47° ±47°	L:6.1×6.6[3] H: 10×7	21.3 24.1	>42	65.4[4] 59.6	No[5]
This work	HW-VICTS	12.5/4% 20.4/7.8%	±49° ±59°	L: 8.12×5.7[3] H: 13.25×9.4	26.1 30.4	>30	85.5[4] 82.3	Yes

[1]λ_0 is the free space wavelength at the center frequency of each passband. [2]L: Low passband, H: High passband. [3]Size of effective radiation region. [4]The values are calculated based on the effective radiation apertures at different operating frequency bands. [5]It is a dual-band combined-aperture VICTS antenna.

non-uniform SWS region in this design. For simplicity, a rectangular region is used in this work. This leads to much smaller radiation aperture than the physical aperture size. Considering the effective radiating aperture size of 195 mm × 136.8 mm (marked out in Fig. 15), the maximum aperture efficiency is up to 85.5%/82.3%.

C. Comparison With Other Work

Table I compares this work with other published VICTS antennas. All the works are based on HW structure. [34] and [35] only support single-band operation, whereas [37], [38] and this work operate at two frequency bands. [37] obtained a large beam coverage (about 60°) only in one frequency band. Although [38] achieved relatively large beam steering ranges of ±47° in both bands, it is based on a combined aperture structure with no radiation aperture reuse. To the best of the authors' knowledge, this work is the first to achieve a dual-band VICTS antenna with large beam coverage in both frequency bands. Within a relative rotation angle of 40°, the beam coverage at center frequencies exceeds 49° in the elevation plane. In addition, this VICTS antenna obtains the highest antenna aperture efficiency of 82.3% in both bands, while maintaining a stable radiation pattern during beam steering.

V. CONCLUSION

This work demonstrated a novel HW-based dual-band shared-aperture VICTS antenna. By employing the hybrid radiating structure of CTS elements and DWRS based elements, unequal effective periods of the radiation elements have been realized for the two frequency bands. Combined with the non-uniform SWS, the initial beam directions for the two bands are both optimized to be close to the boresight, thereby allowing large beam coverage. A PPW diplexer was used to combine the two channels of plane waves and feed the array from one side. This helps to trade-off the amplitude distribution among the radiation elements. A prototype operating at Ku- and K-bands is designed, fabricated and measured. Experimental results show that the proposed antenna achieves the beam coverage of over 49° in both bands by a relative rotation angle of 40°. During the beam steering, the measured peak gain and antenna efficiency are sustained over 21.1 / 25.2 dBi and 73.8 / 74.3% at both frequency bands. The compactness and unique performance of the dual-band antenna may be a competitive candidate for SOTM (when combined with a polarizer), radars, and V2X communications.

REFERENCES

[1] A. A. Baba, R. M. Hashmi, K. P. Esselle, M. Attygalle and D. Borg, "A millimeter-wave antenna system for wideband 2-D beam steering," *IEEE Trans. Antennas Propag.*, vol. 68, no. 5, pp. 3453-3464, May 2020.

[2] Y. Yu, W. Hong, Z. H. Jiang and H. Zhang, "A hybrid radar system with a phased transmitting array and a digital beamforming receiving array," *IEEE Trans. Antennas Propag.*, vol. 69, no. 4, pp. 1970-1981, Apr. 2021.

[3] C. Song et al., "Passive beam-steering gravitational liquid antennas," *IEEE Trans. Antennas Propag.*, vol. 68, no. 4, pp. 3207-3212, Apr. 2020.

[4] G. Mumcu, M. Kacar and J. Mendoza, "Mm-wave beam steering antenna with reduced hardware complexity using lens antenna subarrays," *IEEE Antennas Wireless Propag. Lett.*, vol. 17, no. 9, pp. 1603-1607, Sep. 2018.

[5] C. -N. Chen et al., "38-GHz phased array transmitter and receiver based on scalable phased array modules with endfire antenna arrays for 5G MMW data links," *IEEE Trans. Microw. Theory Techn.*, vol. 69, no. 1, pp. 980-999, Jan. 2021.

[6] W. Hong et al., "The role of millimeter-wave technologies in 5G/6G wireless communications," *IEEE J. Microw.*, vol. 1, no. 1, pp. 101-122, Jan. 2021.

[7] S. Anguix, A. Araghi, M. Khalily and R. Tafazolli, "Reflectarray antenna design for LEO satellite communications in Ka-band," in 1*5th European Conference on Antennas and Propagation (EuCAP)*, 2021, pp. 1-5

[8] Z. -J. Guo et al., "A planar shared-aperture array antenna with a high isolation for millimeter-wave low earth orbit satellite communication system," *IEEE Trans. Antennas Propag.*, vol. 69, no. 11, pp. 7582-7592, Nov. 2021.

[9] M. Ferrando-Rocher, J. I. Herranz-Herruzo, A. Valero-Nogueira and B. Bernardo-Clemente, "Full-metal K-Ka dual-band shared-aperture array antenna fed by combined ridge-groove gap waveguide," *IEEE Antennas Wireless Propag. Lett.*, vol. 18, no. 7, pp. 1463-1467, Jul. 2019.

[10] D. E. Serup, G. F. Pedersen and S. Zhang, "Dual-band shared aperture reflectarray and patch antenna array for S- and Ka-band," *IEEE Trans. Antennas Propag.*, vol. 70, no. 3, pp. 2340-2345, Mar. 2022.

[11] Z. Yang, K. C. Browning and K. F. Warnick, "High-efficiency stacked shorted annular patch antenna feed for Ku-band satellite communications," *IEEE Trans. Antennas Propag.*, vol. 64, no. 6, pp. 2568-2572, Jun. 2016.

[12] S. Moon, S. Yun, I. Yom and H. L. Lee, "Phased array shaped-beam satellite antenna with boosted-beam control," *IEEE Trans. Antennas Propag.*, vol. 67, no. 12, pp. 7633-7636, Dec. 2019.

[13] Y. R. Ding, Y. J. Cheng, J. X. Sun, L. Wang and T. J. Li, "Dual-band shared-aperture two-dimensional phased array antenna with wide bandwidth of 25.0% and 11.4% at Ku- and Ka-Band," *IEEE Trans. Antennas Propag.*, Early access, 2022. doi: 10.1109/TAP.2022.3146867.

[14] W. -W. Yang, X. -H. Ding, T. -W. Chen, L. Guo, W. Qin and J. -X. Chen, "A shared-aperture antenna for (3.5, 28) GHz terminals with end-fire and broadside steerable beams in millimeter wave band," *IEEE Trans. Antennas Propag.*, Early access, 2022. doi: 10.1109/TAP.2022.3178159.

[15] Y. F. Cao, X. Y. Zhang and Q. Xue, "Compact shared-aperture dual-band dual-polarized array using filtering slot antenna and dual-function

metasurface," *IEEE Trans. Antennas Propag.*, vol. 70, no. 2, pp. 1120-1131, Feb. 2022.

[16] Y. Cheng and Y. Dong, "Dual-broadband dual-polarized shared-aperture magnetoelectric dipole antenna for 5G applications," *IEEE Trans. Antennas Propag.*, vol. 69, no. 11, pp. 7918-7923, Nov. 2021.

[17] S. -W. Qu, S. Lu, C. Ma and S. Yang, "K/Ka dual-band reflectarray subreflector for ring-focus reflector antenna," *IEEE Antennas Wireless Propag. Lett.*, vol. 18, no. 8, pp. 1567-1571, Aug. 2019.

[18] J. Wu, C. Wang and Y. X. Guo, "A compact reflector antenna fed by a composite S/Ka-band feed for 5G wireless communications," *IEEE Trans. Antennas Propag.*, vol. 68, no. 12, pp. 7813-7821, Dec. 2020.

[19] T. Su, X. Yi and B. Wu, "X/Ku dual-band single-layer reflectarray antenna," *IEEE Antennas Wireless Propag. Lett.*, vol. 18, no. 2, pp. 338-342, Feb. 2019.

[20] G. -W. Yang and S. Zhang, "A dual-band shared-aperture antenna with wide-angle scanning capability for mobile system applications," *IEEE Trans. Veh. Technol.*, vol. 70, no. 5, pp. 4088-4097, May 2021.

[21] J. Zhang, X. Li, Z. Qi, Y. Huang and H. Zhu, "Dual-band dual-polarization horn antenna array based on orthomode transducers with high isolation for satellite communication," *IEEE Trans. Antennas Propag.*, Early Access, 2022. doi: 10.1109/TAP.2022.3177473.

[22] J. F. Zhang, Y. J. Cheng and Y. R. Ding, "An S- and V-band dual-polarized antenna based on dual-degenerate-mode feeder for large frequency ratio shared-aperture wireless applications," *IEEE Trans. Antennas Propag.*, vol. 68, no. 12, pp. 8127-8132, Dec. 2020.

[23] C. Mao, S. Gao, Q. Luo, T. Rommel and Q. Chu, "Low-cost X/Ku/Ka-band dual-polarized array with shared aperture," *IEEE Trans. Antennas Propag.*, vol. 65, no. 7, pp. 3520-3527, Jul. 2017.

[24] W. W. Milroy, Continuous transverse stub element devices and methods of making same, U.S. Patent 5 266 961 A, Nov. 30, 1993.

[25] M. Del Mastro et al., "Analysis of circularly polarized CTS arrays," *IEEE Trans. Antennas Propag.*, vol. 68, no. 6, pp. 4571-4582, Jun. 2020.

[26] H. Qiu, X. Yang, Y. Yu, T. Lou, Z. Yin and S. Gao, "Compact beam-scanning flat array based on substrate-integrated waveguide," *IEEE Trans. Antennas Propag.*, vol. 68, no. 2, pp. 882-890, Feb. 2020.

[27] M. Del Mastro, S. Lenzini, R. Sauleau and M. Ettorre, "Equidispersive dual-mode long slot arrays," *IEEE Antennas Wireless Propag. Lett.*, vol. 19, no. 12, pp. 2127-2131, Dec. 2020.

[28] Y. Gao, T. Hong, W. Jiang, S. Gong and F. Li, "Low-profile wideband CTS array using substrate-integrated waveguide technology for K-band applications," *IEEE Trans. Antennas Propag.*, vol. 67, no. 8, pp. 5711-5716, Aug. 2019.

[29] Y. Li, M. F. Iskander, Z. Zhang and Z. Feng, "A new low cost leaky wave coplanar waveguide continuous transverse stub antenna array using metamaterial-based phase shifters for beam steering," *IEEE Trans. Antennas Propag.*, vol. 61, no. 7, pp. 3511-3518, Jul. 2013.

[30] X. Yang, L. Di, Y. Yu and S. Gao, "Low-profile frequency-scanned antenna based on substrate integrated waveguide," *IEEE Trans. Antennas Propag.*, vol. 65, no. 4, pp. 2051-2056, Apr. 2017.

[31] Y. You, Y. Lu, Q. You, Y. Wang, J. Huang and M. J. Lancaster, "Millimeter-wave high-gain frequency-scanned antenna based on waveguide continuous transverse stubs," *IEEE Trans. Antennas Propag.*, vol. 66, no. 11, pp. 6370-6375, Nov. 2018.

[32] Y. You, Y. Lu, Y. Wang, J. Xu, J. Huang and W. Hong, "Enhanced pencil-beam scanning CTS leaky-wave antenna based on meander delay line," *IEEE Antennas Wireless Propag. Lett.*, vol. 20, no. 9, pp. 1760-1764, Sep. 2021.

[33] G. Zhang, Q. Zhang, Y. Chen and R. D. Murch, "High-scanning-rate and wide-angle leaky-wave antennas based on glide-symmetry goubau line," *IEEE Trans. Antennas Propag.*, vol. 68, no. 4, pp. 2531-2540, Apr. 2020.

[34] A. Wang, L. Yang, X. Yi, X. Li, J. Zhao, and Y. Zhang, "Wireless communication applications of the variable inclination continuous transverse stub array for Ku-band applications," *IET Microw. Antennas Propag.*, vol. 15, no. 6, pp. 644–652, Mar. 2021.

[35] K. Tekkouk, J. Hirokawa, R. Sauleau and M. Ando, "Wideband and large coverage continuous beam steering antenna in the 60-GHz band," *IEEE Trans. Antennas Propag.*, vol. 65, no. 9, pp. 4418-4426, Sep. 2017.

[36] K. Wang, X. Lei, J. Gao, T. Li, and M. Zhao, "A low-sidelobe-level variable inclination continuous transverse stub antenna with two-types stubs," in *IEEE 4th Advanced Information Management, Communicates, Electronic and Automation Control Conference (IMCEC)*, 2021, pp. 1554-1558

[37] R. S. Hao, Y. J. Cheng, and Y. F. Wu, "Shared-aperture variable inclination continuous transverse stub antenna working at K- and Ka-band for mobile satellite communication," *IEEE Trans. Antennas Propag.*, vol. 68, no. 9, pp. 6656-6666, Sep. 2020.

[38] Y. Lu, Y. You, Y. Wang, Z.-W. Zheng, and J. Huang, "Dual-band combined-aperture variable inclination continuous transverse stub antenna with consistent beam direction," *IEEE Trans. Antennas Propag.*, Early access, 2022. doi: 10.1109/TAP.2022.3177502